

1 **Improving the Thermosphere Ionosphere in a Whole**
2 **Atmosphere Model by Assimilating GOLD Disk**
3 **Temperatures**

4 **F. I. Laskar¹, N. M. Pedatella², M. V. Codrescu³, R. W. Eastes¹, W. E.**
5 **McClintock¹,**

6 ¹Laboratory for Atmospheric and Space Physics, University of Colorado, Boulder, CO, USA

7 ²High Altitude Observatory, National Center for Atmospheric Research, Boulder, CO, USA

8 ³Space Weather Prediction Center, NOAA, Boulder, CO, USA

9 **Key Points:**

- 10 • A new approach has been developed to assimilate GOLD T_{disk} in WACCMX which
11 is validated using independent measurements.
- 12 • Analysis states of both the thermosphere and ionosphere show improved agree-
13 ment with independent measurements.
- 14 • Results demonstrate a great potential of the GOLD T_{disk} data to improve under-
15 standing of the thermosphere ionosphere.

Abstract

Global-scale Observations of Limb and Disk (GOLD) disk measurements of far ultraviolet molecular nitrogen band emissions are used to retrieve column integrated disk temperatures (T_{disk}), which are representative of the lower-and-middle thermosphere. The present work develops a new approach to assimilate the T_{disk} in the Whole Atmosphere Community Climate Model with thermosphere-ionosphere eXtension (WACCMX) using the Data Assimilation Research Testbed (DART) ensemble adjustment Kalman filter. A total of 9 days of data during 1 to 9 November 2018 are assimilated. Analysis state variables such as thermospheric effective temperature (T_{eff}), ratio of atomic oxygen to molecular nitrogen column densities (O/N_2), and column electron content are compared with a control simulation that is only constrained up to ~ 50 km. It is observed that assimilation of the GOLD T_{disk} improves the analysis states when compared with the control simulation. The analysis states, particularly, T_{eff} , O/N_2 , and column electron contents are also compared with their measurement counterparts for the validation of the assimilation. T_{eff} and O/N_2 are compared with GOLD T_{disk} and O/N_2 . While, the Electron Column Density (ECD) from the analyses is compared with ground based Total Electron Content (TEC) measurements from Global Navigational Satellite System (GNSS) receivers. Root Mean Square Error (RMSE) improvements in T_{eff} and O/N_2 are about 12.8% and 13.2%, respectively. The RMSE improvement in analyses ECD is about 8% compared to control simulation.

Plain Language Summary

Understanding of the temperature and density variability of the thermosphere-ionosphere system is very important for satellite drag calculations and satellite communication. The thermosphere-ionosphere system is influenced by waves from the lower atmosphere and solar and geomagnetic forcing from above. For the characterization of this coupled system, realistic whole atmosphere ionosphere parameters are of great interest. The GOLD satellite mission provides daytime thermospheric temperature observations with unprecedented local time and spatial coverage. Including them with the lower and middle atmospheric observations in a whole atmosphere data assimilation system, we find that they improve the state of the thermosphere-ionosphere. This shows the promise of the GOLD disk temperatures in improving thermosphere-ionosphere states and their potential use to improve space weather forecast capabilities.

1 Introduction

Improvements in the satellite drag forecasts and satellite communication depend on a better understanding of the thermosphere-ionosphere (TI) system variability. Earth's TI system is coupled to the lower atmosphere by wave-dynamical forcing and to the solar and geomagnetic forcing from above. The lower atmospheric forcing also varies with location and time. Thus, for a better understanding of this coupled system, a global four dimensional dataset with good temporal and spatial resolution is needed. Satellite measurements from low-Earth orbit can provide good spatial coverage, but they lack local time coverage, unless a constellation of satellites is used. Ground based observations on the other hand have good local time coverage, but they are not available globally due to the significant fraction of the Earth that is covered by ocean. Moreover, the currently available whole atmosphere ionosphere thermosphere observations have data gaps at different altitudes and geographic locations. However, the currently available observations and state-of-the-art whole atmosphere model simulations can be combined in a data assimilation framework. Data assimilation combines observations with model forecasts to produce analysis states that can better estimate the current state of the TI system.

With time the whole atmosphere ionosphere thermosphere models are improving, and the TI system and lower atmosphere observations are increasing. Therefore, we are in a great stage to do a whole atmosphere data assimilation by combining the models and the observations. There is a long-history of lower atmosphere data assimilation (Rienecker et al., 2011; Gelaro et al., 2017; Hersbach et al., 2020), but the whole atmosphere system data assimilation is relatively new. There have been significant developments in the assimilation of thermosphere-ionosphere observations such as, neutral density (Ren & Lei, 2020; M. V. Codrescu et al., 2004; Matsuo et al., 2013; S. M. Codrescu et al., 2018; Sutton, 2018; Mehta et al., 2018), thermospheric temperature (Laskar, Pedatella, et al., 2021), thermospheric airglow irradiance (Cantrall et al., 2019), and electron content (Bust et al., 2004; Lee et al., 2012; Datta-Barua et al., 2013; Matsuo et al., 2013; Lin et al., 2015; Aa et al., 2016; Chen et al., 2016; Bust & Immel, 2020; Pedatella et al., 2020; He et al., 2020; Kodikara et al., 2021; Song et al., 2021; Forsythe et al., 2021). While these results were promising and showed that the assimilation of TI observations improves the model states, most were limited to using upper atmosphere only models or used limited thermospheric datasets from low-earth-orbit satellites or ionospheric only measurements or observing system simulation experiments. Furthermore, a majority of them have not

81 combined lower, middle, and upper atmosphere data in the assimilation. Also, the spa-
 82 tial and temporal coverage of thermospheric data available earlier were limited.

83 Temperature is one of the basic parameters in whole atmosphere models. Neutral
 84 temperature retrieved from Global-scale Observations of Limb and Disk (GOLD) disk
 85 measurements have increased the number of thermospheric observation dramatically, which
 86 enables a whole atmosphere data assimilation that can improve the specification of the
 87 TI system. Laskar, Pedatella, et al. (2021) performed a set of Observing System Sim-
 88 ulation Experiments (OSSEs) to evaluate the impact of assimilating GOLD T_{disk} ob-
 89 servations on thermospheric temperature and dynamics. They found that the OSSE that
 90 includes the GOLD T_{disk} improved the model temperature root mean square error (RMSE)
 91 and bias by 5% and 71% when compared with the forecast state, and the improvements
 92 are 20% and 94% when compared with lower atmosphere only assimilation. Laskar, Pe-
 93 datella, et al. (2021) also found that the migrating diurnal tide (DW1) and local diur-
 94 nal tide over Americas improve by about 8% and 17%, respectively, upon assimilation
 95 of GOLD disk temperature (T_{disk}) observations. In the current study we assimilate ac-
 96 tual GOLD T_{disk} in a whole atmosphere data assimilation system and assess their im-
 97 pact on the thermosphere-ionosphere parameters by validating analysis states with their
 98 measurement counterparts.

99 2 Data, Models, and Methodology

100 The primary dataset used is the GOLD T_{disk} , which has been assimilated in the
 101 Whole Atmosphere Community Climate Model with thermosphere-ionosphere eXten-
 102 sion (WACCMX). In addition to T_{disk} , lower and middle atmosphere data have also been
 103 assimilated. For validation of the analysis states from the assimilation system, indepen-
 104 dent measurements of GOLD O/N₂ and Global Navigation Satellite System Total Elec-
 105 tron Content (GNSS-TEC) are also used. Further details of these data and models are
 106 given below.

107 2.1 GOLD T_{disk}

108 GOLD observed the Earth’s thermosphere in the far ultraviolet wavelengths for over
 109 18.5 hours each day, from 0610 to 0040 Universal Time (UT) of the next day (Eastes et
 110 al., 2019, 2020; McClintock et al., 2020; Laskar et al., 2020). The primary GOLD ob-

111 observations are emission intensities in the far ultraviolet (FUV) range of 134.5 to 166.5
 112 nm. Data for one full disk are available at every 30 minutes from 6-23 UT (Eastes et al.,
 113 2019, 2020; Laskar, Eastes, et al., 2021). The current investigation uses level 2 T_{disk} data
 114 (version 3) that are retrieved from 2×2 binned level-1C data, which are available in the
 115 GOLD web-page, <https://gold.cs.ucf.edu/> as ‘Level 2 - TDISK’. The retrieval al-
 116 gorithm is an improvement of the previously used methods for limb measurements (Aksnes
 117 et al., 2006; Krywonos et al., 2012).

118 The 2×2 binned data have a spatial resolution of $250\text{-km} \times 250\text{-km}$ near nadir. The
 119 GOLD daytime disk scans in N_2 Lyman-Birge-Hopfield (LBH) bands are used to retrieve
 120 T_{disk} data. Effective altitude and contribution function (CF) of the T_{disk} varies with
 121 solar zenith angle (SZA) and emission angle (EA). The SZA variation of the CF is well
 122 quantified (Laskar, Pedatella, et al., 2021) and thus is included in the present assimi-
 123 lation. However, the EA effects are not yet included in the assimilation. But, it has been
 124 observed that the EA does not impact the CF for EAs below 50° , so the T_{disk} data hav-
 125 ing $EA > 50^\circ$ are not included in this assimilation and analysis. This limit also restricts
 126 the latitude and longitude coverage, as shown in Figure 1, to about $\pm 50^\circ$ in latitude and
 127 about $-10^\circ W$ to $-90^\circ W$ in longitude. Also, for high SZA observations the signal to noise
 128 ratio (SNR) is low, which for the current V3 T_{disk} introduces a bias. Thus, the low SNR
 129 observations having $SZA > 65^\circ$ are not considered in the analysis and assimilation.

130 2.2 GOLD O/N₂

131 GOLD disk measurements of OI-135.6 nm emission and N_2 -LBH bands in the ~ 134 -
 132 162 nm wavelength range are used to retrieve the ratio of atomic oxygen to molecular
 133 nitrogen column densities ($\Sigma O / \Sigma N_2$) (Correira et al., 2020). For simplicity we use the
 134 notation O/N₂ instead of $\Sigma O / \Sigma N_2$. The disk O/N₂ has the same spatial and temporal
 135 coverage as that of the T_{disk} . O/N₂ data are used here only for the comparison and val-
 136 idation of the analyses O/N₂. We use the 2×2 binned version 3 O/N₂ data, named as
 137 ‘Level 2 - ON2’ in the GOLD data repository. Also, as the GOLD O/N₂ is not optimized
 138 for auroral latitudes (Correira et al., 2020), the latitudes above $\pm 60^\circ$ are not used in the
 139 current analysis.

2.3 GNSS-TEC

The GNSS-TEC data used in this study are obtained from the madrigal database (<https://cedar.openmadrigal.org>). Madrigal TEC maps are derived from worldwide GNSS ground-based receivers. The vertical TEC data are available at 5 min temporal and 1° by 1° spatial bins. Details on the TEC retrieval algorithm can be found in Rideout and Coster (2006) and Vierinen et al. (2016). In the current study the TEC maps are averaged over 20 minutes centered at every UT hour to compare them with the analysis ECD from assimilation. The 20 minutes averaging is chosen to get enough satellite passes over a particular spatial grid.

2.4 WACCMX

The WACCMX version 2.1 is a whole atmosphere general circulation model extending from the surface to the upper thermosphere (~ 500 - 700 km depending on solar activity) (Liu et al., 2018). WACCMX includes the chemical, dynamical, and physical processes that are necessary to model the lower, middle, and upper atmospheres. The thermosphere and ionosphere processes in WACCMX are similar to those in the NCAR Thermosphere-Ionosphere-Electrodynamics General Circulation Model (TIE-GCM), including the transport of O^+ and self-consistent electrodynamics as well as realistic solar and geomagnetic forcing. The model horizontal resolution is $1.9^\circ \times 2.5^\circ$ in latitude and longitude, and the vertical resolution is 0.25 scale heights above ~ 50 km.

2.5 SD-WACCMX

In this simulation the WACCMX horizontal winds and temperature are relaxed towards Modern-Era Retrospective analysis for Research and Applications, Version 2 (MERRA2) (Gelaro et al., 2017; Rienecker et al., 2011), so we name it as Specified Dynamics WACCMX (SD-WACCMX). The relaxation or nudging to MERRA2 is up to 50 km altitude, and the model is free-running above this altitude (Marsh, 2011). The SD-WACCMX is used in this study as a control simulation. In addition to MERRA2, SD-WACCMX simulations (often referred here as SD-EXP) also use operational solar F10.7 cm flux and geomagnetic Kp index for forcing and thus they can be used as a control simulation for the assessment of the data assimilation states.

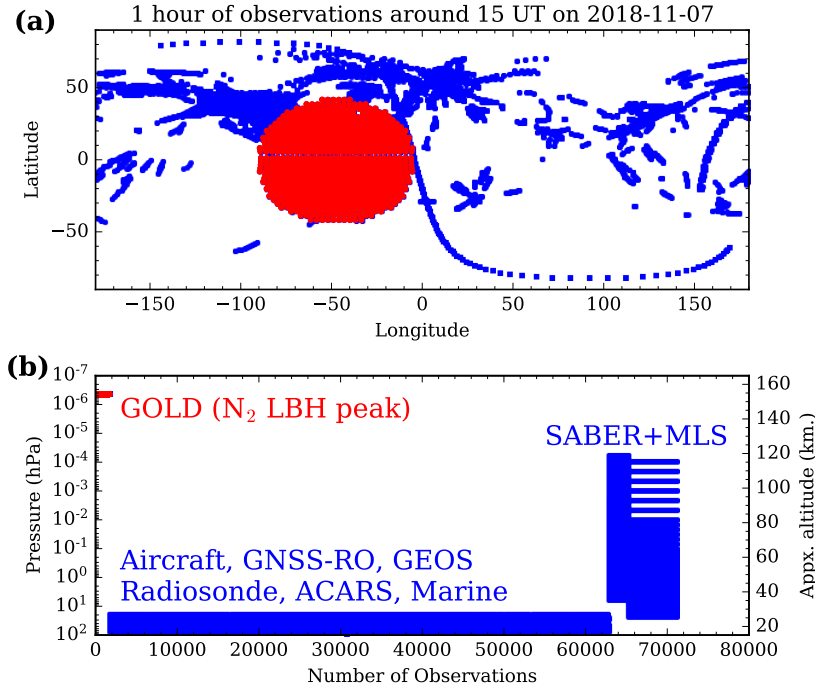


Figure 1. Geo-locations (a), altitude or pressure and number of observations (b) that are assimilated successfully during a representative hour on a particular day are shown. The red points show the GOLD observations and blue points are the rest of the observations, which we term as lower atmosphere observations including SABER and MLS.

169 2.6 WACCMX+DART

170 The data assimilation capability in WACCMX was initially implemented by Pedatella
 171 et al. (2018) using DART (J. Anderson et al., 2009), which uses the ensemble adjustment
 172 Kalman filter (J. L. Anderson, 2001). In the present work we assimilate lower and mid-
 173 dle atmosphere as well as thermosphere observations in the WACCMX+DART. The lower
 174 atmosphere measurements include conventional meteorological observations (i.e., tem-
 175 peratures and winds from aircraft, radiosonde measurements, etc.), as well as GNSS ra-
 176 dio occultation refractivity. Assimilation of these observations improves specifications
 177 of the troposphere-stratosphere globally, which is important for the studies of the ver-
 178 tical coupling of waves from lower-atmosphere to the thermosphere (Wang et al., 2011;
 179 Pedatella et al., 2014; McCormack et al., 2017; Pedatella et al., 2018).

180 In addition to lower altitude observations, middle atmosphere temperatures from
 181 Sounding of the Atmosphere using Broadband Emission Radiometry (SABER) instru-

182 ment on the Thermosphere Ionosphere Mesosphere Energetics and Dynamics (TIMED)
 183 satellite and Aura Microwave Limb Sounder (Aura-MLS) are also used. Altitude cov-
 184 erage of temperature profiles extends from stratosphere to mesosphere-lower-thermosphere
 185 (MLT) altitudes (~ 15 - 105 km for TIMED-SABER and ~ 15 - 90 km for Aura-MLS). The
 186 latitude coverage of TIMED-SABER retrieved temperature alternates between 83°S - 52°N
 187 (south viewing mode) and 83°N - 52°S (north-viewing mode) (Remsberg et al., 2008). We
 188 performed 9 days (1 to 9 November 2018) of data assimilation, during which TIMED-
 189 SABER was in the north-viewing mode on 1 November only. From 2 to 9 November it
 190 was in the south viewing mode. While for the Aura-MLS it varies from 82°S - 82°N (Schwartz
 191 et al., 2008). Though Aura-MLS and TIMED-SABER temperatures are middle atmo-
 192 spheric observations, for simplicity we refer to them here as part of lower atmosphere
 193 observations. Assimilation of these data has previously been demonstrated to improve
 194 specification of the MLT state and dynamics (Pedatella et al., 2014; McCormack et al.,
 195 2017; Laskar et al., 2019).

196 In addition to lower atmosphere observations, GOLD T_{disk} are used in the whole
 197 atmosphere assimilation. As the thermospheric dynamics can change fast in response to
 198 changes in forcing conditions, we use a 1 hour assimilation frequency. Additionally, Pedatella
 199 et al. (2020) have shown that using a 1 hr data assimilation cycle and removal of second-
 200 order divergence damping in WACCMX+DART significantly improves tidal amplitudes,
 201 which were previously found to be too small (Pedatella et al., 2018). Also, the lower at-
 202 mosphere analysis states in WACCMX+DART agree well with other lower atmospheric
 203 assimilations, for example, MERRA2 (McCormack et al., 2021).

204 Figure 1 shows the locations (in a) and altitude or pressure vs. number of obser-
 205 vations (in b) that are assimilated successfully during a representative hour on a par-
 206 ticular day. The red points show the GOLD observations and blue points are the rest
 207 of the observations, which we term as lower atmosphere observations, including TIMED-
 208 SABER and Aura-MLS. Note that the peak altitude of the N_2 -LBH emission is shown
 209 here as a representative altitude of about 150 km, but in the assimilation the impact of
 210 T_{disk} is distributed over altitudes based on the SZA dependent CF (Laskar, Pedatella,
 211 et al., 2021). One can see that about 70000 observations per hour are assimilated. On
 212 an average about 1.5 million observations per day are assimilated. The simulations used
 213 in this study are listed in Table 1. The SD-WACCMX is used in this study as the con-
 214 trol simulation.

Experiment	Observations Assimilated	Nudging Used	Model States Updated
SD-EXP (SD-WACCMX, Control Expt.)	N/A	MERRA2 U, V, T up to 50 km	N/A
DA-EXP1 (WACCMX +DART E1)	Meteorological, Aura-MLS-T, SABER-T, GOLD-T _{disk}	N/A	T
DA-EXP2 (WACCMX +DART E2)	Same as DA EXP1	N/A	T, O, O ₂ , O ⁺

Table 1. WACCMX simulation and data assimilation experiments used in this study are listed. U, V, T, N/A, SD, and DA stands for zonal wind, meridional wind, temperature, Not Applicable, Specified Dynamics, and Data Assimilation, respectively. Also, O, O₂, and O⁺ refers to the mass mixing ratio of atomic oxygen, molecular oxygen, oxygen ion, respectively. The short forms of the experiments are presented in bold.

215 We have performed two WACCMX+DART assimilations. One that assimilates lower
216 atmosphere and GOLD T_{disk} observations and the direct impact of T_{disk} has been re-
217 stricted only to the model temperature, referred to as DA-EXP1 in Table 1. The sec-
218 ond experiment assimilates the same observations as the first experiment but the T_{disk}
219 observations directly impact the model T, O, O₂, and O⁺, referred to as DA-EXP2 in
220 Table 1. We used 40 ensemble members in the assimilation. In order to achieve sufficient
221 spread in the ensemble members, we used a gaussian distribution of solar and geomag-
222 netic forcing parameters with mean as the actual value with standard deviations of 15
223 sfu for F10.7 cm flux and 1 for Kp index. We reset any F10.7 value less than 60 sfu to
224 60 sfu and any negative Kp to 0. The forcing perturbations for a particular ensemble re-
225 mains same for all the days. To avoid artifacts arising from initial ensemble members
226 the spinup duration for the two assimilation runs are about 2 weeks.

3 Results

In order to assess and validate the performance of the assimilation we compare the ensemble averaged analysis states to their measurement counterparts. For example, effective temperature (T_{eff}) from model simulation is compared with GOLD T_{disk} ; O/N_2 is compared with GOLD O/N_2 ; and Electron Column Density (ECD) is compared with the GNSS-TEC. Note that T_{eff} here refers to the vertically integrated GOLD equivalent temperature that is calculated by integrating the model temperature profile weighted by the SZA dependent CFs. Also, the ECD is similar to TEC, but the column integration is only to the topmost layer of WACCMX, which is about 480 km for the current case. Figure 2 shows a comparison of the local time and latitude variation of the GOLD T_{disk} with T_{eff} from ensemble averaged states of the DA-EXP1 (DA-EXP1 T_{eff}) and SD-WACCMX (SD-EXP T_{eff}) for 2 different days. The latitudes and local times are restricted to only those locations and times where GOLD T_{disk} is being assimilated. Beyond those local time and latitudes GOLD data are available but we are not using them in the assimilation as explained in Sections 2.1 and 2.2. Note that in this figure only a representative longitude of $48^\circ W$ is shown, which is close to the sub-satellite point of GOLD.

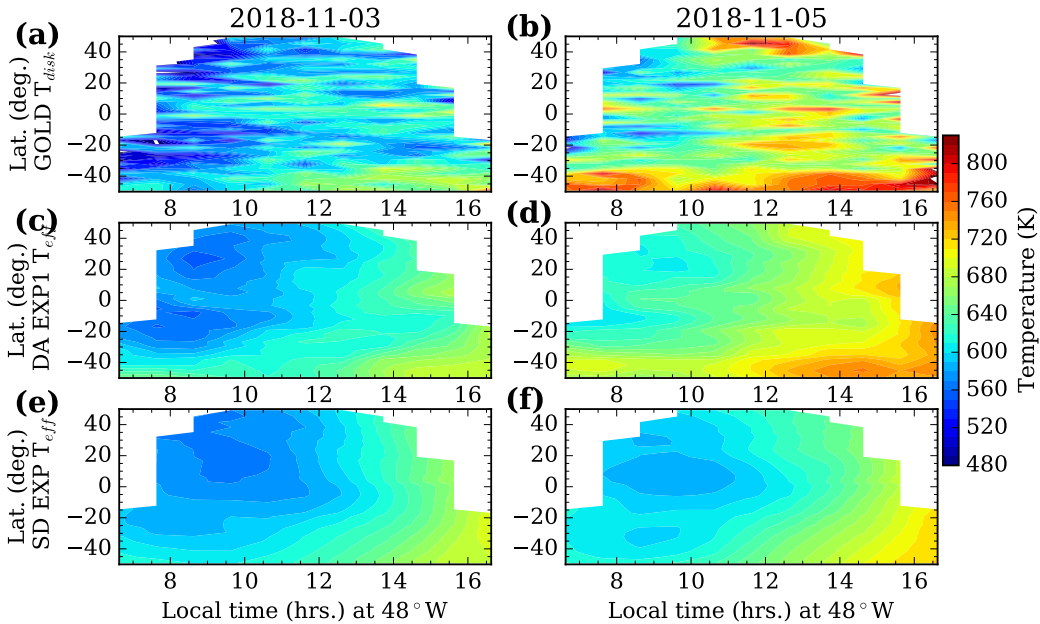


Figure 2. Local time and latitude variation of the GOLD T_{disk} compared with T_{eff} from DA-EXP1 (DA-EXP1 T_{eff}) and SD-WACCMX (SD-EXP T_{eff}).

243 It can be noted from Figure 2 that the broad variations between T_{disk} and DA-
 244 EXP1 T_{eff} are similar on both the days. On 5th November 2018 there was a moderate
 245 geomagnetic storm for which the average temperature is more than 100 K higher than
 246 3rd November 2018. Moreover, the morning temperatures are relatively warmer, partic-
 247 ularly between 40° and 50°S. These variations of the GOLD T_{disk} during geomagnetic
 248 events have been reported and discussed in Laskar, Eastes, et al. (2021). On both days
 249 the small scale local time features in T_{disk} can also be seen in DA-EXP1 T_{eff} , but they
 250 are absent in SD-EXP T_{eff} . This suggests that the data assimilation is driving the model
 251 temperature in the right direction. Quantitative estimate of the differences between them
 252 are given later. Note that since both the assimilation experiments updated the temper-
 253 ature directly at every assimilation step, the T_{eff} are nearly the same for both cases.
 254 So, the T_{eff} for only the DA-EXP1 is shown here.

255 The variation in temperature also changes other states by altering the model dy-
 256 namics. Therefore assimilation of T_{disk} can also impact the O/N₂ ratio, which is another
 257 primary dataset from the GOLD. Figure 3 shows a comparison of GOLD O/N₂ with the
 258 O/N₂ from data assimilation and control simulation experiments, for the same 2 days
 259 shown in Figure 2. Unlike Figure 2, here the latitude range is extended to 60°N/S, as
 260 the GOLD O/N₂ are valid for those latitudes. We compare O/N₂ from the DA-EXP1
 261 (c and d), DA-EXP2 (e and f), and SD-EXP (g and h) with the GOLD O/N₂ (a and b).
 262 Note that the GOLD O/N₂ observations have not been assimilated in any of the exper-
 263 iments. In the DA-EXP2 the GOLD T_{disk} observations also directly update the O, O₂,
 264 and O⁺ mass mixing ratios in addition to temperature. The direct updating of these quan-
 265 tities impacts the neutral composition and ionosphere at every assimilation step and thus
 266 they are expected to compare better than the indirectly updated states. It can be ob-
 267 served from Figure 3 that the broad variations in O/N₂ agree well between GOLD O/N₂
 268 and the two assimilation experiments. Though interhemispheric features in SD-EXP, the
 269 assimilation experiments, and the observations match well there are clear differences in
 270 finer structures between them. For the quiet-day of 3rd November the two assimilation
 271 experiments show better agreement with GOLD O/N₂ compared to the SD-EXP O/N₂.
 272 The highest discrepancy in O/N₂ can be seen on the storm day (right panel) where the
 273 Northern higher-latitude depletion in the GOLD O/N₂ is nearly absent in SD-EXP and
 274 is weak in the two assimilation runs.

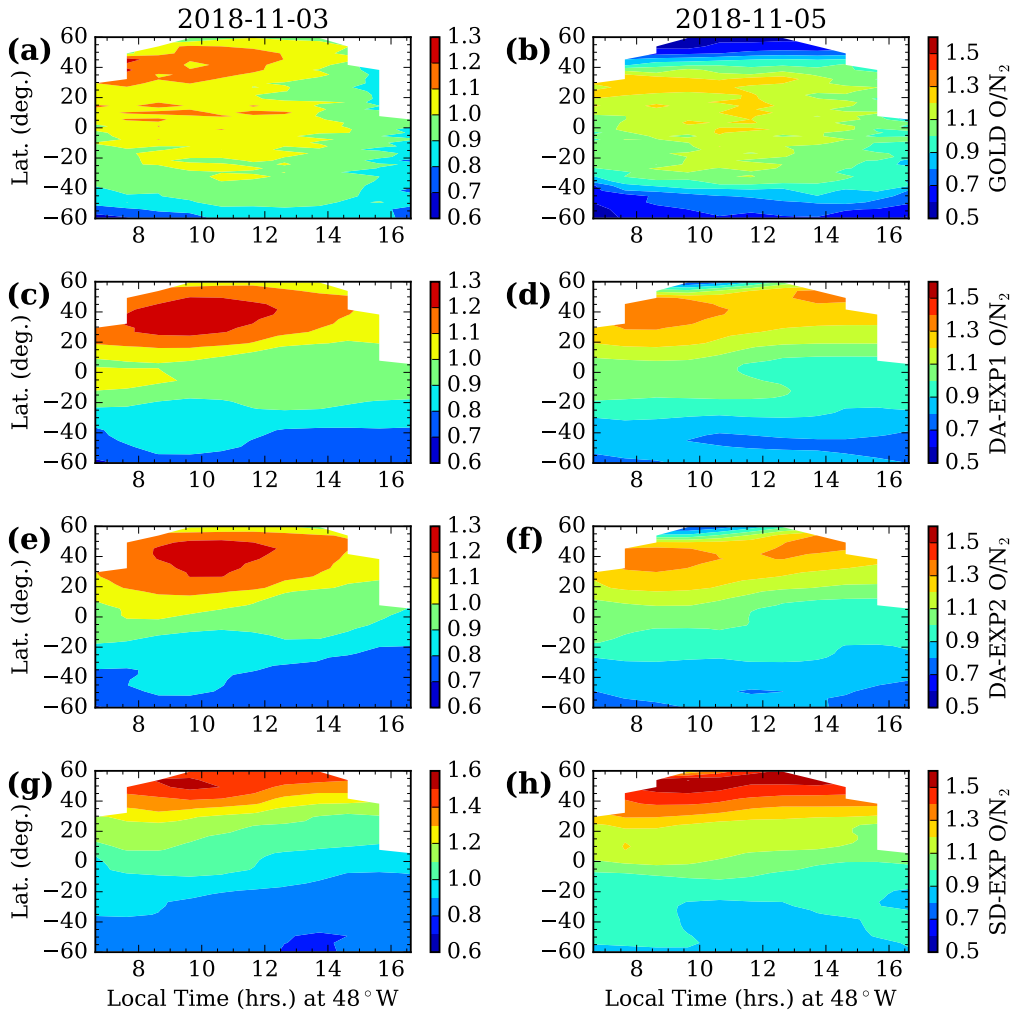


Figure 3. Same as Figure 2 but for the column integrated O/N₂ ratio. In addition to the DA-EXP1 the DA-EXP2 O/N₂ is also shown in (e and f).

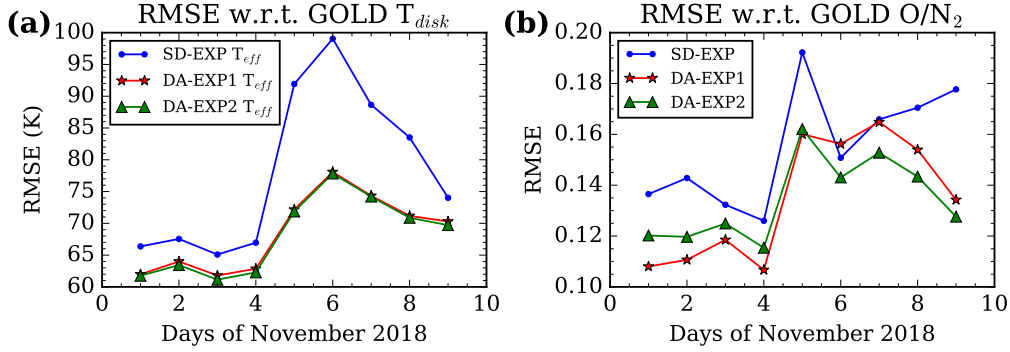


Figure 4. The RMSEs in DA-EXP1 T_{eff} and DA-EXP2 T_{eff} with respect to GOLD T_{disk} are shown in (a) and similar RMSEs in O/N_2 are shown in (b). Note that the temperature RMSEs in the two data assimilation runs, are clearly smaller than the SD-EXP. Also, the average O/N_2 RMSEs are better for the two assimilation runs compared to the SD-EXP.

275 For a quantitative estimation of the above observed differences between actual mea-
 276 surements and their data assimilation equivalents we calculate the Root Mean Square
 277 Error (RMSE). The RMSE in SD-EXP T_{eff} , DA-EXP1 T_{eff} , and DA-EXP2 T_{eff} with
 278 respect to GOLD T_{disk} are shown in Figure 4(a) for all the 9 days. The RMSE for each
 279 day is calculated over the whole disk and local time range as shown in Figure 2 for tem-
 280 perature and Figure 3 for O/N_2 . Note that the temperature RMSEs in the two data as-
 281 similation runs are clearly smaller than the SD-EXP. Also, the temperature RMSE for
 282 the two assimilation runs are almost same, which is expected as both the assimilations
 283 updated model temperature directly. The RMSEs in O/N_2 are shown in Figure 4(b). The
 284 average O/N_2 RMSEs are better for the two assimilation runs compared with the SD-
 285 EXP. The pre-storm RMSEs are smaller compared with storm onset and recovery phase.
 286 Average RMSE improvements in effective temperature and O/N_2 compared to the SD-
 287 EXP are about 12.8% and 13.2%, respectively. The improvements of pre-storm RMSE
 288 in T_{disk} and O/N_2 are about 6.4% and 11.3% while during the storm they were about
 289 18.8% and 11.5%, respectively.

290 For a more robust diagnosis of the relationship between SD-EXP T_{eff} , DA-EXP1
 291 T_{eff} , and DA-EXP2 T_{eff} with respect to GOLD T_{disk} for all the available latitudes,
 292 longitudes in the disk scans between 10 to 20 UT during 1 to 9 November 2018 we make
 293 scatter diagrams as shown in Figure 5, where the red color represents high density points.

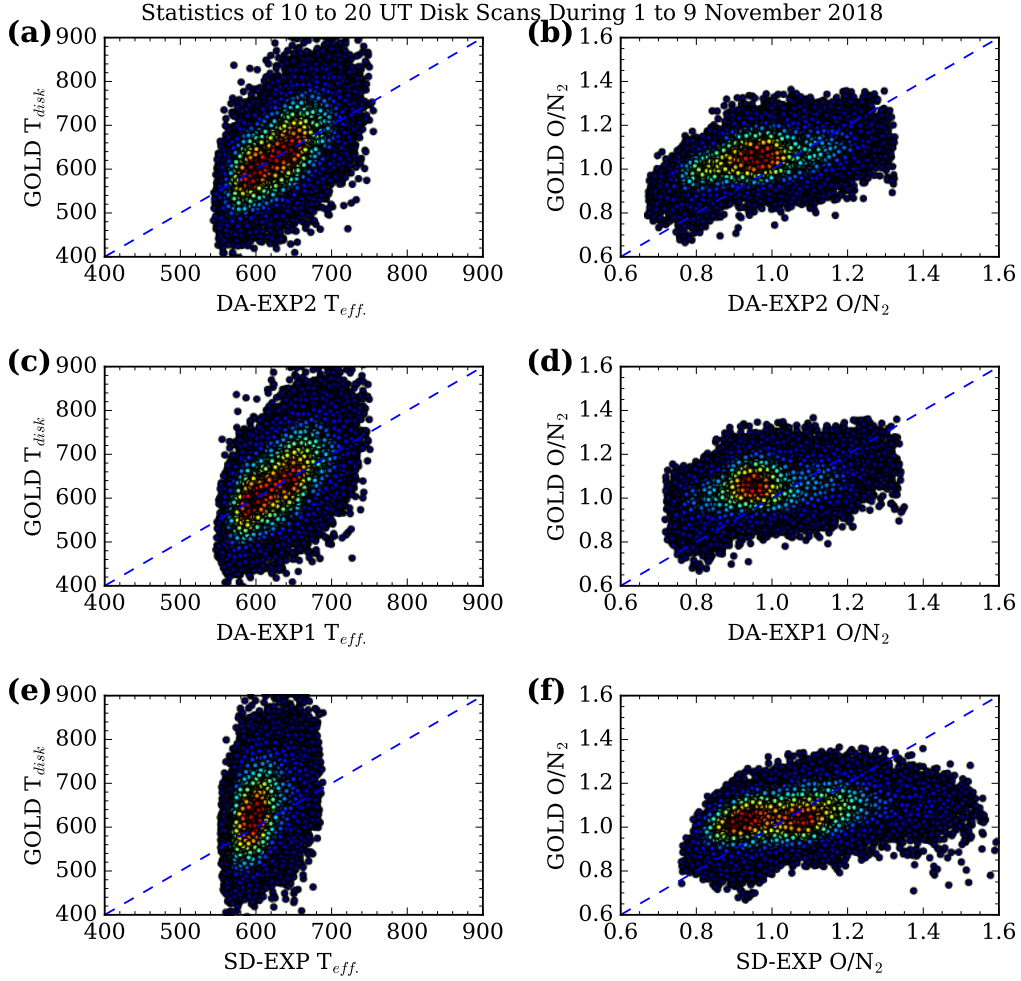


Figure 5. Scatter diagram of the GOLD T_{disk} and O/N_2 compared to their DA-EXP2, DA-EXP1, and SD-EXP equivalents are shown. For this analysis all the disk scans between 10 to 20 UT during 1 to 9 Nov. 2018 are used. The red regions in the scatter diagram represents highest density points. For the GOLD vs. DA-EXP2 the highest density points distribute around the linear 45° slope line, particularly for the temperature. The comparison w.r.t. SD-EXP for both temperature and O/N_2 , on the other hand, is not so good.

294 From these scatter plots it can be seen that the majority of the T_{disk} vs. DA-EXP2 T_{eff}
 295 points (in a) fall just over the linear correlation straight line with slope 45° . But, for the
 296 T_{disk} vs. SD-EXP T_{eff} (in e) comparison, the highest density observations (red points)
 297 deviate away from the linear fit with 45° slope. Note that here also, only those obser-
 298 vations are shown that fall within the 50° EA and 65° SZA limits. As the GOLD T_{disk}
 299 has higher spread compared to DA-EXP2 T_{eff} , DA-EXP1 T_{eff} , and SD-EXP T_{eff} the
 300 shape of the scatter plot is elongated towards the T_{disk} axis (in a, c, and e). Similar to
 301 temperature, the O/N_2 scatter diagrams are shown in Figure 5(b, d, and f) but the EA
 302 and SZA restrictions are not applied here. Here also, the agreement of GOLD O/N_2 with
 303 DA-EXP2 O/N_2 (in b) is better compared with the GOLD vs. SD-EXP O/N_2 (in f).
 304 Though, the agreement for GOLD vs. DA-EXP2 O/N_2 is less than that of T_{disk} vs. DA-
 305 EXP2 T_{eff} , but there is significant improvement when compared with GOLD vs. SD-
 306 EXP O/N_2 . The distribution of points in the GOLD T_{disk} vs. DA-EXP1 T_{eff} and GOLD
 307 T_{disk} vs. DA-EXP2 T_{eff} is nearly identical because the temperature was updated di-
 308 rectly in both the assimilations. However, the distributions in O/N_2 in Figure 5(b and
 309 d) are significantly different. The O/N_2 scatter diagram for the GOLD vs. DA-EXP1
 310 is better than the GOLD vs. SD-EXP but not as good as compared to GOLD vs. DA-
 311 EXP2.

312 The improvements in the O/N_2 motivated us to analyze the electron content de-
 313 rived from the assimilations and compare them with the independent measurements of
 314 GNSS-TEC. Figure 6 shows a latitude vs. day-to-day variation of ECD in SD-EXP (a),
 315 DA-EXP1 (b), DA-EXP2 (c), and GNSS-TEC (d) centered at around $60^\circ W$ ($\pm 5^\circ$) lon-
 316 gitude. This spatial bin has been chosen due to the greater availability of GNSS data
 317 in this region. As mentioned in section 2.3, the GNSS-TEC data are averaged over 20
 318 minutes duration centered at every hour. Note that even with the 20 minute averaging,
 319 there are missing data, specifically between 20° and $40^\circ N$. This figure shows that the mag-
 320 nitudes of electron densities and the shape and temporal variability of Equatorial Ion-
 321 ization Anomaly (EIA) in DA-EXP2 has better agreement with GNSS-TEC compared
 322 to the DA-EXP1 and SD-EXP. Particularly, the northern mid-latitude enhanced DA-
 323 EXP2 ECDs are in better agreement with GNSS-TEC. Though there are improvements
 324 in DA-EXP2, the EIA latitude extent and hemispheric asymmetries are not yet well re-
 325 produced in the assimilations. This could be due to the fact that the temperature vari-
 326 ability cannot fully reflect the changes in the ionosphere as the ionosphere is also influ-

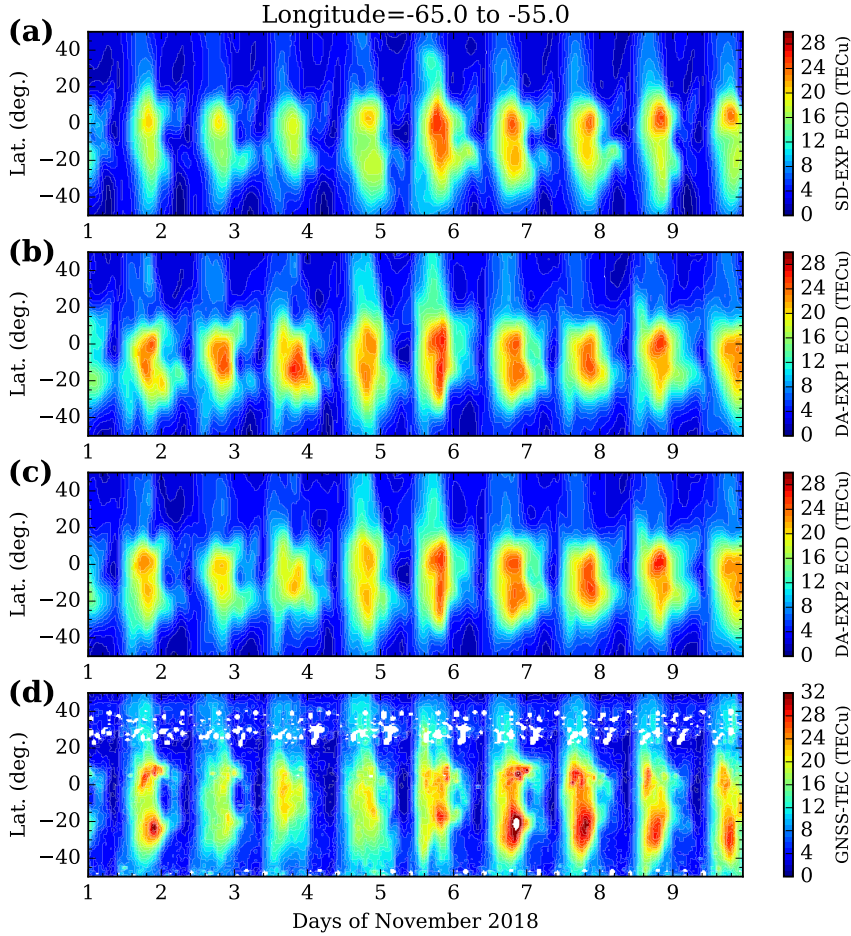


Figure 6. Latitude and day-to-day variability of SD-EXP ECD (a), DA-EXP1 ECD (b), DA-EXP2 ECD (c), and GNSS-TEC (d) averaged over 55°W to 65°W longitude.

327 ended by neutral and ionospheric composition changes. We expect to have better agree-
 328 ment in the future when the GOLD O/N₂ and other ionospheric dataset are assimilated
 329 in addition to the T_{disk} .

330 For a qualitative assessment of the improvements seen in the ionospheric electron
 331 content, a comparison between SD-ECD (green), DA-EXP1 ECD (cyan), DA-EXP2 ECD
 332 (red), and GNSS-TEC (blue) for a limited spatial region is shown in Figure 7(a). Also,
 333 the RMSE (in Figure 7b) and bias (in Figure 7c) with respect to GNSS-TEC are also shown.
 334 The DA-EXP2 ECD has better agreement with GNSS-TEC as can be inferred from the
 335 smaller values of the RMSE and bias. Some of the local time variabilities also have bet-

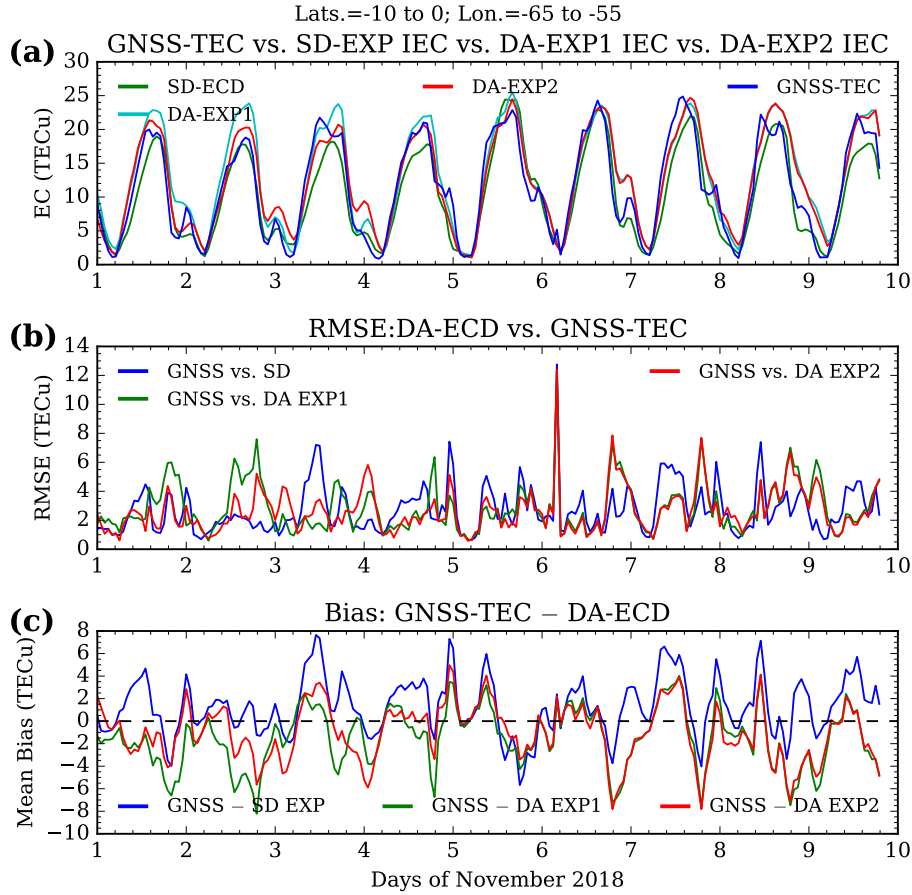


Figure 7. (a) Comparison of the SD-EXP ECD (green), DA-EXP1 ECD (cyan), DA-EXP2 ECD (red), and GNSS-TEC (blue) which are averaged over 10°S to 0°N and 55°W to 65°W . (b) RMSEs in GNSS-TEC vs. SD-EXP ECD (blue), GNSS-TEC vs. DA-EXP1 ECD (green), and GNSS-TEC vs. DA-EXP2 ECD (red). (c) Mean bias in GNSS-TEC vs. SD-EXP ECD (blue), GNSS-TEC vs. DA-EXP1 ECD (green), and GNSS-TEC vs. DA-EXP2 ECD (red) are shown.

336 ter agreement with DA-EXP2. For example, the two-peak structures in daytime GNSS-
 337 TEC on days 1, 3, 4, 5, and 9 are better reproduced in the DA-EXP2 ECD. Also, the
 338 broader shape of the local time variability in GNSS-TEC match better with DA-EXP2
 339 ECD as can be seen on most days in Figure 7(a). Most of the higher RMSEs in DA oc-
 340 cur during night-time sector, where GOLD T_{disk} observations are not available. The pur-
 341 pose of this comparison is to demonstrate that the ionosphere is also improved upon as-
 342 similation of GOLD T_{disk} . From Figure 7(c) it can be noted that the mean bias is also
 343 lower for the DA-EXP2 ECD. A quantitative estimate of the differences, that varies with
 344 latitude and time, are given below.

345 In Figure 3 we show that the GOLD O/N_2 has latitudinal differences from the DA
 346 O/N_2 . Also, we have seen in Figure 6 that the agreement between DA-EXP2 ECD and
 347 GNSS-TEC varies with latitude. To investigate these latitudinal differences in TEC we
 348 have calculated the RMSE and mean bias at every 10 degree latitude bin during the 9
 349 days. The RMSE and mean bias in electron contents from SD-EXP, DA-EXP1, and DA-
 350 EXP2 with respect to GNSS TEC are shown in Figure 8. One can note that the low-
 351 est values of the RMSE and bias are observed for the DA-EXP2, the red lines marked
 352 with stars. The RMSE and bias at every latitude bin is calculated from all the $24 \times 9 = 216$
 353 hours of data. The percentage improvements in RMSE for DA-EXP1 ECD and DA-EXP2
 354 ECD with respect to GNSS-TEC are about 3% and 8%, respectively. The 9 day aver-
 355 age mean biases with respect to GNSS-TEC for the SD-EXP, DA-EXP1, and DA-EXP2
 356 are about 1.9, 0.5, and 0.8 TECu, respectively. Though the latitudinal average of the
 357 mean biases is slightly smaller for the DA-EXP1 compared to DA-EXP2, it is clear that
 358 the biases are smaller for both the assimilations compared to SD-EXP. Also, the the mean
 359 bias is positive at higher latitudes ($> 30^\circ$) as seen in Figure 8(b). Since the O/N_2 and
 360 TEC vary in proportion, the lower O/N_2 (from GOLD as shown in Figure 3(b)) at the
 361 higher latitudes compared to SD and DA experiments produce the positive mean biases
 362 in TEC. These results further emphasize that the DA-EXP2 – where in addition to tem-
 363 perature the O, O^+ , and O_2 mixing ratios are updated directly – improves the thermo-
 364 sphere and ionosphere. Overall, it can be observed that the RMSEs are lower in the North-
 365 ern hemisphere compared to the Southern hemisphere, which suggests that the North-
 366 ern hemispheric variabilities are better reproduced in the assimilation.

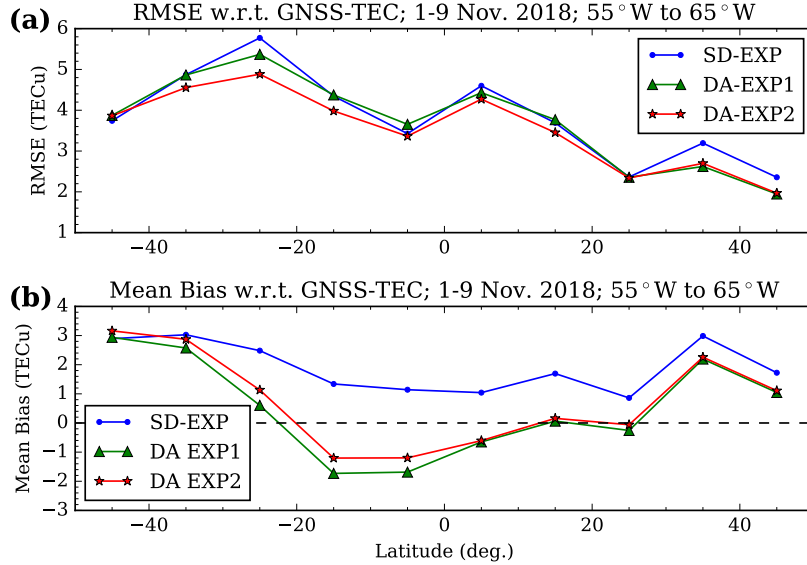


Figure 8. Latitudinal variability of RMSE (a) and mean bias (b) for SD-EXP (blue), DA-EXP1 (green), and DA-EXP2 (red) with respect to GNSS-TEC during 1-9 Nov. 2018 are shown. Clearly, for the DA-EXP2 the RMSE is smaller compared to other two cases and bias is closer to zero.

367 4 Conclusions

368 An investigation of the impact of GOLD T_{disk} assimilation on thermosphere-ionosphere
 369 states is carried out using WACCMX+DART. The salient results of this investigation
 370 are:

- 371 1. GOLD T_{disk} assimilation analysis states of the thermosphere-ionosphere show bet-
 372 ter agreement with independent measurements than the control simulation.
- 373 2. The GOLD T_{disk} and O/N_2 compare better with the WACCMX+DART effec-
 374 tive temperature and O/N_2 when compared with equivalent parameters from SD-
 375 WACCMX.
- 376 3. The RMSE improvements in analyses effective temperature and O/N_2 , when com-
 377 pared to GOLD measurements, are about 12.8% and 13.2%, respectively.
- 378 4. The RMSE between GNSS-TEC and analysis electron column density (ECD) is
 379 better compared to that between GNSS-TEC and SD-WACCMX ECD. The im-
 380 provement in this is about 8% for the assimilation that updates the O, O^+ , and
 381 O_2 densities in addition to temperature.

382 These results indicate that the GOLD observations of the thermospheric temper-
 383 ature has a great potential to improve the operational and short term forecast of the thermosphere-
 384 ionosphere system.

385 Acknowledgments

386 This research was supported by NASA Contract 80GSFC18C0061 to the University of
 387 Colorado, Boulder. This material is also based upon work supported by the National Cen-
 388 ter for Atmospheric Research (NCAR), which is a major facility sponsored by the Na-
 389 tional Science Foundation under Cooperative Agreement No. 1852977. Computing and
 390 data storage resources, including the Cheyenne supercomputer ([https://doi.org/10](https://doi.org/10.5065/D6RX99HX)
 391 [.5065/D6RX99HX](https://doi.org/10.5065/D6RX99HX)), were provided by the Computational and Information Systems Lab-
 392 oratory (CISL) at NCAR. WACCMX is part of the Community Earth System Model (CESM)
 393 and the source code is available at <http://www.cesm.ucar.edu>. DART is available at
 394 <https://www.image.ucar.edu/DAReS/DART/>. The Level 2 data used in this study are
 395 available at the GOLD Science Data Center (<https://gold.cs.ucf.edu/search/>) and
 396 at NASA's Space Physics Data Facility ([https://spdf.gsfc.nasa.gov/pub/data/gold/](https://spdf.gsfc.nasa.gov/pub/data/gold/level2/tdisk/)
 397 [level2/tdisk/](https://spdf.gsfc.nasa.gov/pub/data/gold/level2/tdisk/)). The assimilation and simulation data used in this work are available
 398 at <https://doi.org/10.5281/zenodo.5546491>.

399 References

- 400 Aa, E., Liu, S., Huang, W., Shi, L., Gong, J., Chen, Y., . . . Li, J. (2016, June).
 401 Regional 3-d ionospheric electron density specification on the basis of data as-
 402 simulation of ground-based GNSS and radio occultation data. *Space Weather*,
 403 *14*(6), 433–448. doi: 10.1002/2016sw001363
- 404 Aksnes, A., Eastes, R., Budzien, S., & Dymond, K. (2006). Neutral temperatures
 405 in the lower thermosphere from N₂ Lyman-Birge-Hopfield (LBH) band profiles.
 406 *Geophysical Research Letters*, *33*(15). doi: 10.1029/2006gl026255
- 407 Anderson, J., Hoar, T., Raeder, K., Liu, H., Collins, N., Torn, R., & Avellano, A.
 408 (2009, September). The data assimilation research testbed: A community fa-
 409 cility. *Bulletin of the American Meteorological Society*, *90*(9), 1283–1296. doi:
 410 10.1175/2009bams2618.1
- 411 Anderson, J. L. (2001, December). An ensemble adjustment kalman filter for data
 412 assimilation. *Monthly Weather Review*, *129*(12), 2884–2903. doi: 10.1175/1520

- 413 -0493(2001)129(2884:aeakff)2.0.co;2
- 414 Bust, G. S., Garner, T. W., & Gaussiran II, T. L. (2004). Ionospheric data as-
 415 simulation three-dimensional (IDA3D): A global, multisensor, electron density
 416 specification algorithm. *Journal of Geophysical Research: Space Physics*,
 417 *109*(A11). doi: 10.1029/2003ja010234
- 418 Bust, G. S., & Immel, T. J. (2020, March). IDA4D: Ionospheric data assimilation
 419 for the ICON mission. *Space Science Reviews*, *216*(3). doi: 10.1007/s11214-020-
 420 -00648-z
- 421 Cantrall, C. E., Matsuo, T., & Solomon, S. C. (2019, October). Upper atmosphere
 422 radiance data assimilation: A feasibility study for GOLD far ultraviolet obser-
 423 vations. *Journal of Geophysical Research: Space Physics*, *124*(10), 8154–8164.
 424 doi: 10.1029/2019ja026910
- 425 Chen, C. H., Lin, C. H., Matsuo, T., Chen, W. H., Lee, I. T., Liu, J. Y., . . . Hsu,
 426 C. T. (2016, June). Ionospheric data assimilation with thermosphere-
 427 ionosphere-electrodynamics general circulation model and GPS-TEC dur-
 428 ing geomagnetic storm conditions. *Journal of Geophysical Research: Space*
 429 *Physics*, *121*(6), 5708–5722. doi: 10.1002/2015ja021787
- 430 Codrescu, M. V., Fuller-Rowell, T. J., & Minter, C. F. (2004, November). An
 431 ensemble-type kalman filter for neutral thermospheric composition during
 432 geomagnetic storms. *Space Weather*, *2*(11). doi: 10.1029/2004sw000088
- 433 Codrescu, S. M., Codrescu, M. V., & Fedrizzi, M. (2018, January). An ensemble
 434 kalman filter for the thermosphere-ionosphere. *Space Weather*, *16*(1), 57–68.
 435 doi: 10.1002/2017sw001752
- 436 Correira, J., Lumpe, J. D., Evans, J. S., Kyrwonos, A., Veibell, V., McClintock,
 437 W. E., & Eastes, R. (2020). Thermospheric composition and solar euv flux
 438 from the global-scale observations of the limb and disk (gold) mission. *Earth*
 439 *and Space Science Open Archive*, *31*. doi: 10.1002/essoar.10501920.2
- 440 Datta-Barua, S., Bust, G. S., & Crowley, G. (2013, November). First storm-time
 441 plasma velocity estimates from high-resolution ionospheric data assimilation.
 442 *Journal of Geophysical Research: Space Physics*, *118*(11), 7458–7471. doi:
 443 10.1002/2013ja019153
- 444 Eastes, R. W., McClintock, W. E., Burns, A. G., Anderson, D. N., Andersson,
 445 L., Aryal, S., . . . Woods, T. N. (2020, June). Initial observations by the

- 446 GOLD mission. *Journal of Geophysical Research: Space Physics*, *125*(7). doi:
447 10.1029/2020ja027823
- 448 Eastes, R. W., Solomon, S. C., Daniell, R. E., Anderson, D. N., Burns, A. G., Eng-
449 land, S. L., . . . McClintock, W. E. (2019, August). Global-scale observations
450 of the equatorial ionization anomaly. *Geophysical Research Letters*, *46*(16),
451 9318–9326. doi: 10.1029/2019gl084199
- 452 Forsythe, V. V., Azeem, I., Blay, R., Crowley, G., Makarevich, R. A., & Wu,
453 W. (2021, April). Data assimilation retrieval of electron density pro-
454 files from ionosonde virtual height data. *Radio Science*, *56*(5). doi:
455 10.1029/2021rs007264
- 456 Gelaro, R., McCarty, W., Suárez, M. J., Todling, R., Molod, A., Takacs, L., . . .
457 Zhao, B. (2017, July). The modern-era retrospective analysis for research and
458 applications, version 2 (MERRA-2). *Journal of Climate*, *30*(14), 5419–5454.
459 doi: 10.1175/jcli-d-16-0758.1
- 460 He, J., Yue, X., Le, H., Ren, Z., & Wan, W. (2020, March). Evaluation on the
461 quasi-realistic ionospheric prediction using an ensemble kalman filter data
462 assimilation algorithm. *Space Weather*, *18*(3). doi: 10.1029/2019sw002410
- 463 Hersbach, H., Bell, B., Berrisford, P., Hirahara, S., Horányi, A., Muñoz-Sabater,
464 J., . . . Thépaut, J.-N. (2020, June). The ERA5 global reanalysis. *Quar-
465 terly Journal of the Royal Meteorological Society*, *146*(730), 1999–2049. doi:
466 10.1002/qj.3803
- 467 Kodikara, T., Zhang, K., Pedatella, N. M., & Borries, C. (2021, May). The im-
468 pact of solar activity on forecasting the upper atmosphere via assimilation of
469 electron density data. *Space Weather*, *19*(5). doi: 10.1029/2020sw002660
- 470 Krywonos, A., Murray, D. J., Eastes, R. W., Aksnes, A., Budzien, S. A., & Daniell,
471 R. E. (2012, September). Remote sensing of neutral temperatures in the
472 Earth’s thermosphere using the Lyman-Birge-Hopfield bands of N₂: Compar-
473 isons with satellite drag data. *Journal of Geophysical Research: Space Physics*,
474 *117*(A9). doi: 10.1029/2011ja017226
- 475 Laskar, F. I., Eastes, R. W., Codrescu, M. V., Evans, J. S., Burns, A. G., Wang,
476 W., . . . Cai, X. (2021, August). Response of GOLD retrieved thermospheric
477 temperatures to geomagnetic activities of varying magnitudes. *Geophysical
478 Research Letters*, *48*(15). doi: 10.1029/2021gl093905

- 479 Laskar, F. I., Eastes, R. W., Martinis, C. R., Daniell, R. E., Pedatella, N. M., Burns,
480 A. G., . . . Codrescu, M. V. (2020, July). Early morning equatorial ionization
481 anomaly from GOLD observations. *Journal of Geophysical Research: Space*
482 *Physics*, *125*(7). doi: 10.1029/2019ja027487
- 483 Laskar, F. I., McCormack, J. P., Chau, J. L., Pallamraju, D., Hoffmann, P., &
484 Singh, R. P. (2019, August). Interhemispheric meridional circulation dur-
485 ing sudden stratospheric warming. *Journal of Geophysical Research: Space*
486 *Physics*, *124*(8), 7112–7122. doi: 10.1029/2018ja026424
- 487 Laskar, F. I., Pedatella, N. M., Codrescu, M. V., Eastes, R. W., Evans, J. S., Burns,
488 A. G., & McClintock, W. (2021, January). Impact of GOLD retrieved thermo-
489 spheric temperatures on a whole atmosphere data assimilation model. *Journal*
490 *of Geophysical Research: Space Physics*, *126*(1). doi: 10.1029/2020ja028646
- 491 Lee, I. T., Matsuo, T., Richmond, A. D., Liu, J. Y., Wang, W., Lin, C. H., . . .
492 Chen, M. Q. (2012). Assimilation of formosat-3/cosmic electron density
493 profiles into a coupled thermosphere/ionosphere model using ensemble kalman
494 filtering. *Journal of Geophysical Research: Space Physics*, *117*(A10). doi:
495 <https://doi.org/10.1029/2012JA017700>
- 496 Lin, C. Y., Matsuo, T., Liu, J. Y., Lin, C. H., Tsai, H. F., & Araujo-Pradere,
497 E. A. (2015, January). Ionospheric assimilation of radio occultation and
498 ground-based GPS data using non-stationary background model error co-
499 variance. *Atmospheric Measurement Techniques*, *8*(1), 171–182. doi:
500 10.5194/amt-8-171-2015
- 501 Liu, H.-L., Bardeen, C. G., Foster, B. T., Lauritzen, P., Liu, J., Lu, G., . . . Wang,
502 W. (2018, February). Development and validation of the whole atmosphere
503 community climate model with thermosphere and ionosphere extension
504 (WACCM-x 2.0). *Journal of Advances in Modeling Earth Systems*, *10*(2),
505 381–402. doi: 10.1002/2017ms001232
- 506 Marsh, D. R. (2011). Chemical–dynamical coupling in the mesosphere and lower
507 thermosphere. In *Aeronomy of the earths atmosphere and ionosphere* (pp. 3–
508 17). Springer Netherlands. doi: 10.1007/978-94-007-0326-1_1
- 509 Matsuo, T., Lee, I.-T., & Anderson, J. L. (2013, March). Thermospheric mass den-
510 sity specification using an ensemble kalman filter. *Journal of Geophysical Re-*
511 *search: Space Physics*, *118*(3), 1339–1350. doi: 10.1002/jgra.50162

- 512 McClintock, W. E., Eastes, R. W., Beland, S., Bryant, K. B., Burns, A. G., Cor-
 513 reira, J., . . . Veibel, V. (2020, May). Global-scale observations of the limb
 514 and disk mission implementation: 2. observations, data pipeline, and level 1
 515 data products. *Journal of Geophysical Research: Space Physics*, *125*(5). doi:
 516 10.1029/2020ja027809
- 517 McCormack, J. P., Harvey, V. L., Pedatella, N., Koshin, D., Sato, K., Coy, L., . . .
 518 Holt, L. A. (2021). Intercomparison of middle atmospheric meteorological
 519 analyses for the northern hemisphere winter 2009-2010. *Atmospheric Chem-*
 520 *istry and Physics Discussions*, *2021*, 1–48. doi: 10.5194/acp-2021-224
- 521 McCormack, J. P., Hoppel, K., Kuhl, D., de Wit, R., Stober, G., Espy, P., . . . Hi-
 522 bbins, R. (2017, February). Comparison of mesospheric winds from a high-
 523 altitude meteorological analysis system and meteor radar observations during
 524 the boreal winters of 2009–2010 and 2012–2013. *Journal of Atmospheric and*
 525 *Solar-Terrestrial Physics*, *154*, 132–166. doi: 10.1016/j.jastp.2016.12.007
- 526 Mehta, P. M., Linares, R., & Sutton, E. K. (2018, May). A quasi-physical dy-
 527 namic reduced order model for thermospheric mass density via hermitian
 528 space-dynamic mode decomposition. *Space Weather*, *16*(5), 569–588. doi:
 529 10.1029/2018sw001840
- 530 Pedatella, N. M., Anderson, J. L., Chen, C. H., Raeder, K., Liu, J., Liu, H.-L., &
 531 Lin, C. H. (2020, September). Assimilation of ionosphere observations in the
 532 whole atmosphere community climate model with thermosphere-ionosphere
 533 EXtension (WACCMX). *Journal of Geophysical Research: Space Physics*,
 534 *125*(9). doi: 10.1029/2020ja028251
- 535 Pedatella, N. M., Liu, H.-L., Marsh, D. R., Raeder, K., Anderson, J. L., Chau, J. L.,
 536 . . . Siddiqui, T. A. (2018, April). Analysis and hindcast experiments of the
 537 2009 sudden stratospheric warming in WACCMX+DART. *Journal of Geophys-*
 538 *ical Research: Space Physics*, *123*(4), 3131–3153. doi: 10.1002/2017ja025107
- 539 Pedatella, N. M., Raeder, K., Anderson, J. L., & Liu, H.-L. (2014, August). Ensem-
 540 ble data assimilation in the whole atmosphere community climate model. *Jour-*
 541 *nal of Geophysical Research: Atmospheres*, *119*(16), 9793–9809. doi: 10.1002/
 542 2014jd021776
- 543 Remsberg, E. E., Marshall, B. T., Garcia-Comas, M., Krueger, D., Lingenfelter,
 544 G. S., Martin-Torres, J., . . . Thompson, R. E. (2008, September). Assessment

- 545 of the quality of the version 1.07 temperature-versus-pressure profiles of the
546 middle atmosphere from TIMED/SABER. *Journal of Geophysical Research*,
547 *113*(D17). doi: 10.1029/2008jd010013
- 548 Ren, D., & Lei, J. (2020, August). Evaluation of physics-based data assimilation
549 system driven by neutral density data from a single satellite. *Space Weather*,
550 *18*(8). doi: 10.1029/2020sw002504
- 551 Rideout, W., & Coster, A. (2006, May). Automated GPS processing for global total
552 electron content data. *GPS Solutions*, *10*(3), 219–228. doi: 10.1007/s10291-006
553 -0029-5
- 554 Rienecker, M. M., Suarez, M. J., Gelaro, R., Todling, R., Bacmeister, J., Liu, E., ...
555 Woollen, J. (2011, July). MERRA: NASA’s modern-era retrospective analysis
556 for research and applications. *Journal of Climate*, *24*(14), 3624–3648. doi:
557 10.1175/jcli-d-11-00015.1
- 558 Schwartz, M. J., Lambert, A., Manney, G. L., Read, W. G., Livesey, N. J., Froide-
559 vaux, L., ... Wu, D. L. (2008, May). Validation of the aura microwave limb
560 sounder temperature and geopotential height measurements. *Journal of Geo-
561 physical Research*, *113*(D15). doi: 10.1029/2007jd008783
- 562 Song, R., Hattori, K., Zhang, X., & Yoshino, C. (2021, August). The three-
563 dimensional ionospheric electron density imaging in japan using the approx-
564 imate kalman filter algorithm. *Journal of Atmospheric and Solar-Terrestrial
565 Physics*, *219*, 105628. doi: 10.1016/j.jastp.2021.105628
- 566 Sutton, E. K. (2018, June). A new method of physics-based data assimilation for
567 the quiet and disturbed thermosphere. *Space Weather*, *16*(6), 736–753. doi: 10
568 .1002/2017sw001785
- 569 Vierinen, J., Coster, A. J., Rideout, W. C., Erickson, P. J., & Norberg, J. (2016,
570 March). Statistical framework for estimating GNSS bias. *Atmospheric Mea-
571 surement Techniques*, *9*(3), 1303–1312. doi: 10.5194/amt-9-1303-2016
- 572 Wang, H., Fuller-Rowell, T. J., Akmaev, R. A., Hu, M., Kleist, D. T., & Iredell,
573 M. D. (2011, December). First simulations with a whole atmosphere data
574 assimilation and forecast system: The january 2009 major sudden stratospheric
575 warming. *Journal of Geophysical Research: Space Physics*, *116*(A12). doi:
576 10.1029/2011ja017081